HHS Public Access

Author manuscript

Neuron. Author manuscript; available in PMC 2017 March 16.

Published in final edited form as:

Neuron. 2016 March 16; 89(6): 1317–1330. doi:10.1016/j.neuron.2016.02.020.

A role for synaptic input distribution in a dendritic computation of motion direction in the retina

Anna L. Vlasits[1], **Ryan D. Morrie**[2], **Alexandra Tran-Van-Minh**[3,4], **Adam Bleckert**[5], **Christian F. Gainer**[6], **David A. DiGregorio**[3,4], and **Marla B. Feller**[1,2]

[1]Helen Wills Neuroscience Institute, University of California, Berkeley, CA 94720, USA

[2]Department of Molecular and Cell Biology, University of California, Berkeley, CA 94720, USA

[3]Unit of Dynamic Neuronal Imaging, Institut Pasteur, 75724, Paris, France

[4]Centre National de la Recherche Scientifique (CNRS), UMR 3571, Genes, Synapses and Cognition, 75724, Paris, France

[5]Department of Biological Structure, University of Washington, Seattle, WA 98195, USA

[6]Department of Optometry, University of California, Berkeley, CA 94704, USA

Summary

The starburst amacrine cell in the mouse retina presents an opportunity to examine the precise role of sensory input location on neuronal computations. Using visual receptive field mapping, glutamate uncaging, two-photon Ca^{2+} imaging, and genetic labeling of putative synapses, we identify a unique arrangement of excitatory inputs and neurotransmitter release sites on starburst amacrine cell dendrites: the excitatory input distribution is skewed away from the release sites. By comparing computational simulations with Ca^{2+} transients recorded near release sites, we show that this anatomical arrangement of inputs and outputs supports a dendritic mechanism for computing motion direction. Direction selective Ca^{2+} transients persist in the presence of a GABA-A receptor antagonist, though the directional tuning is reduced. These results indicate a synergistic interaction between dendritic and circuit mechanisms for generating direction selectivity in the starburst amacrine cell.

Introduction

Starburst amacrine cells (SACs) are axonless GABAergic interneurons, whose release sites are located in the distal tips of their processes. SACs play a critical in the computations of direction selectivity by providing asymmetric inhibition onto direction selective ganglion cells (DSGCs), which fire selectively to motion in one direction and very little to motion in

Contact should be addressed to DAD (; Email: david.digregorio@pasteur.fr) and MBF (; Email: mfeller@berkeley.edu)

Author contributions

ALV and MBF designed the receptive field experiments. ALV performed receptive field mapping and analysis. ALV, DD, ATVM and MBF designed uncaging experiments. ALV and ATVM performed uncaging experiments. ALV analyzed uncaging experiments. RDM, ALV and CG performed Ca^{2+} imaging. RDM and ALV analyzed Ca^{2+} imaging. AB designed, performed, and analyzed the PSD95 experiments. AB and ALV performed comparison of output sites, PSD95 and uncaging data. ATVM and DD created the starburst cell simulation. All authors wrote the manuscript.

the other direction (Amthor et al., 2002; Fried et al., 2002, 2005; Vlasits et al., 2014; Yoshida et al., 2001). The mechanism of direction selective inhibition from SACs has been widely studied. DSGCs receive greater inhibitory input from SACs located on their "null side" (Fried et al., 2002; Wei et al., 2011; Yonehara et al., 2011) due to selective wiring of inhibitory synapses from SAC dendrites pointed in the DSGC's null direction (Beier et al., 2013; Briggman et al., 2011; Morrie and Feller, 2015). But wiring cannot by itself explain direction selective inhibition, because DSGCs exhibit DS even when moving stimuli are restricted to a small region of the receptive field (Fried et al., 2002). Therefore, GABA release from SAC dendrites must also be DS. Indeed, individual SAC dendrites prefer motion in different directions. Specifically, Ca^{2+} transients in SAC dendrites are larger in response to motion outward from the soma to the end of the dendrite compared to motion inward from the end of the dendrite to the soma (Euler et al., 2002; Hausselt et al., 2007; Lee and Zhou, 2006; Yonehara et al., 2013). SACs receive excitatory input from bipolar cells, glutamatergic interneurons that are the major feed-forward circuit component in the retina. But bipolar cell axon terminals exhibit neither DS Ca^{2+} transients (Chen et al., 2014; Yonehara et al., 2013) nor DS glutamate release onto DSGCs (Park et al., 2014). This suggests that the first computation of motion direction takes place in SAC dendrites.

Currently, there are three hypotheses of how direction selective calcium signals arise in SAC dendrites. The first hypothesis is that integration of spatially-offset bipolar cell inputs with different release kinetics produces DS (Kim et al., 2014). The second is that circuit-level reciprocal lateral inhibition between SACs creates a preference for outward motion in the absence of dendrite-intrinsic asymmetries (Lee and Zhou, 2006; Münch and Werblin, 2006). The third is a dendrite-intrinsic mechanism, which proposes that passive properties of SAC dendrites, combined with non-linear conductances, are capable of computing motion direction (see Vaney et al., 2012 for review). However, the precise dendritic computations would depend on the arrangement of input and output sites. Outputs (GABA release sites) are located in the distal 1/3 of the SAC dendrite, where widenings called varicosities contact DSGCs (Briggman et al., 2011; Famiglietti, 1991). On the other hand, different distributions of excitatory inputs have been proposed in the SAC dendritic arbor: either inputs cover the entire arbor (Famiglietti, 1991; Koizumi et al., 2011) or there are fewer inputs in the distal dendrites (Kim et al., 2014).

Here, we determined the dendritic locations of excitatory synaptic inputs to elucidate the dendrite-intrinsic mechanisms that play a role in SAC computations. We utilized several methods to examine the excitatory input distribution: visual receptive field mapping, localized glutamate uncaging, and labeling of the PSD95 distribution. In addition, we modeled the SAC to explore the effect of changing the input distribution on the voltage responses in different regions of the dendrite. Finally, we used two-photon Ca^{2+} imaging of varicosities to determine the relative contributions of excitation and lateral inhibition to the direction selective computation in SAC dendrites.

Results

The starburst amacrine cell excitatory receptive field is excluded from distal dendrites

A neuron's input distribution relative to its outputs can make a difference in the nature of the dendrite-intrinsic computation the cell can perform. If inputs and outputs are comingled, *local* dendritic computations would dominate. On the other hand, if inputs are skewed or segregated away from output sites, *global* computations within each dendrite would dominate (Fig. 1A). Modeling studies thus far have assumed inputs are near to output sites (Taylor and Smith, 2012; Tukker et al., 2004), and achieving DS in this case requires strong nonlinear mechanisms.

To determine the functional map of excitatory inputs onto SAC dendrites in the retina, we first measured the excitatory receptive field using visual stimulation of the retina with small spots (25 μm diameter) whose size was chosen to roughly match the receptive field size of cone bipolar cells (Berntson and Taylor, 2000) (Fig 1B). We performed voltage clamp recordings from SACs to measure light-evoked excitatory currents (Fig. 1C) and quantified the charge transfer as a function of the position of the stimulation spot relative to the dendritic radius. We observed a decrease in charge transfer as spots were presented further from the soma, with spots centered at ≥74±13% of the dendritic radius producing <5% of the maximum charge transfer recorded in the cell (Fig. 1D–E, n = 15 cells). On the other hand, we did not observe differences in the spot response kinetics at different locations on the dendritic tree, suggesting that phasic vs. sustained bipolar cell release kinetics may not play a role in generating DS in On-SACs (Fig. S1; see **Discussion** and Kim et al., 2014). We repeated our receptive field measurements using 24 μm wide ring stimuli to stimulate all of the SAC dendrites at a certain radius on the arbor at once (Fig. 1F). Similar to the stimulation with small spots of light, the charge transfer in response to rings decreased to <5% of the maximum response with rings centered at ≥77±10% (average±S.D. for 6 cells) of the maximum dendritic radius (Fig. 1I). In addition, during stimulation outside of the dendritic field we observed a decrease in the tonic excitatory current that coincided with an inhibitory current; the inhibitory receptive field extended beyond the excitatory receptive field (Fig. S1). Thus, based on ring and spot stimulation, the excitatory receptive field appears to exclude the most distal dendrites.

So far, we have determined the excitatory receptive field using voltage clamp recordings from the soma, but SACs are thought to release neurotransmitter from varicosities in their distal dendrites. To determine the impact of proximal vs. distal visual stimulation at SAC release sites, we performed two-photon imaging of Ca^{2+} transients from varicosities in SACs filled with OGB-1 (Fig. 2A). Consistent with our voltage clamp recordings (Fig. 1), we observed larger Ca^{2+} transients in varicosities in response to spots centered at proximal compared to distal locations, despite the distal spots' closer proximity to the varicosities being imaged (Fig. 2B–E). Together, these findings suggest that the excitatory receptive field does not include distal regions of the dendrites, but nevertheless has a strong influence on the Ca^{2+} concentration there.

Glutamate uncaging reveals absence of excitatory synapses in distal dendrites

To directly characterize the distribution of excitatory inputs on SAC dendrites, we used 2-photon fluorescence imaging, glutamate uncaging by single-photon photolysis of MNI-glutamate (2 mM, bath-applied) (DiGregorio et al., 2007), and somatic voltage clamp recordings (Fig. 3A–B). Locations along the dendrite where uncaging-evoked EPSCs were detected were assumed to result from the presence of AMPAR clusters (Abrahamsson et al., 2012). We selected uncaging-evoked EPSCs with locally-maximal amplitudes as the location of putative postsynaptic sites (Fig. S2). In 20 dendrites from 15 cells, the majority of putative synapses were in the more proximal region of the dendritic tree (Fig. 3C–D), resulting in an excitatory receptive field that extended to 69±9% of the dendritic field, similar to that determined using visual stimulation (Fig. 3E). We confirmed that the lack of responses in distal dendritic regions was not due to alterations in the uncaging resolution or cable filtering (Fig. S3), and therefore not below the sensitivity of our measurements. Taken together, these results are consistent with the conclusion that synaptic inputs are absent from the outer third of the SAC dendritic tree.

PSD95 puncta are skewed away from output sites

We next used an anatomical approach to confirm our functional estimates of the distribution of glutamate receptors in SAC dendrites. Retinas were biolistically transfected with plasmids encoding post-synaptic density 95 fused to YFP (PSD95-YFP) to label putative sites of glutamatergic input and tdTomato for identification of transfected SACs (Fig. 4A, C). We then took confocal images of SAC processes that did not overlap with other labeled cells and identified the locations of PSD95 puncta (Fig. 4B; see Methods and Fig. S4). We found that PSD95 puncta were at the highest density near the soma, while the density decreased more distally with a profile similar to the putative postsynaptic sites detected with uncaging (Fig. 4D, n = 8 cells from 5 retinas).

To establish the locations of inputs relative to outputs, we plotted putative postsynaptic locations determined from uncaging or PSD95 labeling and release sites. We took advantage of data from a previous study that used serial block-face electron microscopy (SBEM) to characterize the dendritic locations of On and Off SAC contacts with DSGCs (Briggman et al., 2011). We found that synaptic input and output distributions were significantly skewed away from one another (Fig. 4E; $p<0.05$, Wilcoxon Rank test). Similarly, only 25% of the output sites overlapped with the excitatory receptive field predicted from uncaging (Fig. 4E, orange dotted line is the mean radial distance of the last postsynaptic site predicted from uncaging). This arrangement of inputs and outputs suggests that computations in the SAC most likely rely on a global mechanism of dendritic integration (Fig. 1A), and may underlie a dendrite-intrinsic DS computation.

Skewed synaptic input distributions enhance DS of simulated dendritic voltage

How does the skewed distribution of inputs contribute to direction selectivity of SAC outputs? To address this question, we turned to a computer simulation based on a passive “ball and stick” representation of the SAC dendrite (Fig. 5A, D and Fig. S5). The dendritic morphology was based on the average lengths of dendritic branches measured from SACs imaged by 2-photon microscopy (data not shown). We compared the dendritic voltage

responses produced by several different input distributions: the skewed distribution determined by uncaging (Fig. 5A), the higher density skewed distribution determined by PSD95 labeling (Fig. S5A), a regular distribution covering the entire dendritic length (Fig. 5D, Fig. S5D), and a regular distribution covering the proximal 71% of the dendritic length, which is the extent of the excitatory receptive field predicted from uncaging (calculated from Fig. 3C). These different distributions allowed us to assess separately the impact of skewed synapse distributions and the effect of the absence of any inputs to the distal region of the SAC.

We simulated voltage along the dendrite during outward and inward stimulation of inputs at an apparent velocity of 500 μm/s and report the results both at specific sites (Fig. 5B, E) as well as continuously along the entire dendrite (Fig. 5C, F). To quantify the strength of DS, we computed the difference in peak depolarization between outward and inward stimulation (Fig. 5H, J). There were three primary predictions from the model. First, we found that input distributions restricted to the proximal 71% of the dendrite (whether skewed distributions or regular distributions) produced the strongest DS for outward motion. Second, input distributions restricted to the proximal 71% of the dendrites also led to lower DS values for varicosities located within the receptive field of the SAC process compared to varicosities located outside the receptive field. Third, the degree of DS was constant over a long section at the end of the dendrite (>30 μm for the uncaging distribution; >45 μm for the PSD95 distribution) only for input distributions restricted to the proximal 71% of the dendrites. The uniform depolarization along the distal dendrite is the result of inputs localized to the proximal portion of the dendritic tree acting in combination with the sealed cable effect of the dendrite (see **Discussion**). In contrast, stimulating a regular synapse distribution covering the whole dendrite produced DS values that became steadily stronger with increasing distance from the soma, although DS remained much weaker than for input distributions restricted to the proximal 71%, even at the most distal sites (Fig. 5G–J). These results were consistent at a faster velocity of stimulation (1000 μm/s, data not shown). Our passive model simulations suggest that a proximal-weighted input distribution promotes a prominent direction selective depolarization in the distal dendritic tips, where the majority of release sites are located.

DS of varicosities depends on varicosity location

Our simulations predict that varicosities in the distal region of the dendrite will have similar strength DS, in contrast to weaker DS at more proximal release sites (Fig. 5). To test this prediction directly, we performed 2-photon Ca^{2+} imaging of varicosities in SACs while stimulating the retina with moving squares of light (25 μm^2). Note, there are two important differences from previous measurements that used Ca^{2+} imaging to assess DS in SAC dendrites (Euler et al., 2002; Hausselt et al., 2007; Lee and Zhou, 2006; Yonehara et al., 2013). First, we stimulated the retina with small moving squares, rather than circular gratings or stimuli larger than the size of the SAC dendritic field, to observe single motion-evoked events and isolate the contribution from a single process. Second, we restricted the moving square to 75% of the dendritic radius to optimally stimulate the excitatory receptive field (Fig. 6A). Similar to previous studies, we observed distal varicosities that responded with Ca^{2+} transients that were larger for outward compared to inward motion (Fig. 6B, C)

and a large variance in the DS across varicosities (Euler et al., 2002; Hausselt et al., 2007; Lee and Zhou, 2006; Yonehara et al., 2013) (Fig. 6F–G). We believe this variance to be due to the complex dendritic structure being stimulated (Fig. S6) or to off-axis tuning of varicosities, as described previously (Euler et al., 2002; Yonehara et al., 2013).

Next, we examined how the DS of a varicosity related to its location along the SAC dendrite. Because our model predicts strong DS of varicosities over the last ~30% of the SAC dendrite, we split the imaged varicosities into two groups using the average path length to the last synapse predicted from uncaging (71% of the dendritic path from the soma, calculated from Fig. 3C). We found that varicosities located distal to the last synapse predicted from uncaging (examples in Fig. 6B, C) were significantly more direction selective than varicosities located within the region where synapses were detected (examples in Fig. 6D, E, summary in Fig. 6F, G; mean DSI = 0.34±0.23 for 25 varicosities outside receptive field and 0.11±0.18 for 8 varicosities inside receptive field; Student's t-test: $p<0.05$). These results demonstrate that the DSI of varicosity Ca^{2+} transients depends on location in a manner consistent with the voltage responses predicted by a purely passive dendrite model.

Excitatory and inhibitory inputs cooperate to enhance DS

While we have demonstrated that the excitatory input distribution can enable a dendrite-intrinsic computation of motion direction, some studies have proposed that lateral inhibition from other SACs is the origin of DS in SAC dendrites (Lee and Zhou, 2006; Münch and Werblin, 2006). Note, lateral inhibition between SACs in adult mice is mostly provided by SAC processes oriented in antiparallel directions (Fig. S7, Kostadinov and Sanes, 2015; Lee and Zhou, 2006). Given this geometry, inward light stimulation for the SAC being recorded would correspond to outward motion for neighboring presynaptic SACs (Fig. S7). Hence, the dendrite-intrinsic computation described above would maximally drive GABA release from the neighboring SAC onto the SAC being recorded, enabling lateral inhibition, which we predict will enhance DS by suppressing responses to inward light stimulation.

To test this model, we conducted two manipulations. First we compared DS in distal varicosities in response to motion stimuli that ended at 75% of the dendritic radius (as in Fig. 6) to those that ended at 100% of the dendritic radius, which is likely to induce a more robust activation of inhibitory inputs because the stimulus travels over a larger portion of the neighboring SACs' dendrites (Fig. S7). Indeed, we observed larger DSIs in response to 100% stimulation compared to 75% stimulation (Fig. 7B, E; paired t-test: $p<0.05$ [Bonferroni corrected], n=22 varicosities). This difference is due primarily to a reduction in Ca^{2+} transients evoked by 100% inward stimulation (Fig. 7D).

Second, we repeated these experiments in the $GABA_A$ receptor antagonist, gabazine (5 μM). Though there was an overall reduction in DSI across varicosities (Fig. 7E; repeated measures ANOVA: $p<0.05$ for control vs. gabazine groups), the majority of varicosities still exhibited larger responses to outward motion compared to inward motion (e.g. Fig. 7C). The weakened DSI in the absence of GABAergic inhibition is primarily attributable to an increase in the response to inward motion (Fig. 7D), suggesting that in control conditions inhibition is more pronounced during inward stimulation. Notably, in the absence of GABAergic network interactions, the enhanced DS observed for 100% stimulation over 75%

was eliminated (Fig. 7F; mean $\Delta DSI_{control} = 0.16 \pm 0.1$; $\Delta DSI_{gabazine} = 0.02 \pm 0.23$). Thus, both excitatory and inhibitory inputs cooperate to compute motion direction in SAC dendrites, and both are greatly enhanced by the differential dendritic distributions of inputs and outputs. Taken together, our results suggest that DS is achieved through a dendrite-intrinsic computation, which determines the outward preference as well as the circuit-level lateral inhibition of the response to inward motion (Fig. S7).

Discussion

Directly linking neural connectivity to neuronal computations is a major goal of contemporary neuroscience. We studied the relationship between excitatory input locations and the motion direction computation that SACs perform. We found that the excitatory inputs are localized to the proximal two-thirds of the dendritic tree, mostly segregated from output sites, and that their distribution can determine the region of the dendrite where varicosities are direction selective. This differential distribution enhances the mechanisms influencing DS; both the intrinsic dendritic mechanism and the lateral inhibition mechanism. These results allowed us to determine the relative contributions from dendrite-intrinsic and circuit-level mechanisms to DS in SAC dendrites. Our findings highlight the critical importance of synaptic input placement and distribution within the dendrite in determining the types of neuronal computations performed.

Excitatory inputs to starburst amacrine cells

We used several approaches to demonstrate that the excitatory input distribution is mostly separated from the varicosity-rich distal dendrites. We observed this distribution in three ways: as a restricted visual receptive field using either voltage clamp recordings from the soma (Fig. 1) or two-photon Ca^{2+} imaging in distal processes (Fig. 2), as a paucity of synapses in distal dendrites detected with glutamate uncaging (Fig. 3), and as a decreased density of PSD95-YFP expression in distal dendrites (Fig. 4). These findings are consistent with a SBEM study that found fewer bipolar cell contacts in the most distal dendrites, albeit in Off-layer SACs (Kim et al., 2014).

Our results indicate that there may be a different distribution of glutamate receptors in mice than in rabbit, where several studies determined that excitatory inputs are present throughout the entire SAC dendritic tree. These studies also used a variety of methods, including visual receptive field mapping with ring stimuli and voltage clamp recordings (Lee and Zhou, 2006), electron microscopy (Famiglietti, 1991), and PSD95-GFP labeling (Koizumi et al., 2011). Hence, it appears that a different combination of excitatory and inhibitory distributions may account for DS in rabbit.

Mechanisms of dendritic integration in starburst amacrine cell dendrites

Overall, our findings suggest that the distribution of excitatory inputs in SACs can produce a dendrite-intrinsic DS response, with outward motion producing a larger depolarization in distal varicosities compared to inward motion (Fig. 5–6). We found that DS was strongest for varicosities located outside of the excitatory receptive field and that more proximal varicosities are less direction selective (Fig. 6F,G). Two properties of SAC dendrites are the

basis of this effect: the high input impedance of narrow diameter dendrites and the sealed-end of the distal dendritic compartment, which retards current flow (the “end effect”, see Rall, 1964, 1967).

High input impedance of narrow diameter dendrites contributes to DS in the following way. In somatic recordings of uncaging-evoked currents, we observed a tendency of the rise time to increase and the amplitude to decrease with increasing distance along the dendrite (Fig. S2), although our simulations suggest that the filtering-induced reduction in amplitude is similar for inputs placed 85 or 150 μm from the soma (Fig. S3). Thus, it is highly unlikely that the decreased probability of detecting events in distal dendrites resulted from dendritic filtering. The narrow diameter of the dendrite (<0.3 μm) is likely to account for this filtering over the short distances in SAC dendrites (<150 μm). Numerical simulations indicate that dendritic filtering is critical for producing the slow-rising and -decaying EPSPs in varicosities during stimulation of inputs proximal to the soma (Fig. 5). This filtering produces the sensitivity to outward stimulation, in which larger peak depolarizations are achieved because the proximal inputs, which are distant from release sites, produce slow depolarizations in the release compartments. Outward DS results from activation of synapses progressively closer to release sites, which produces a depolarization that summates on previous EPSPs more distant from release sites, thus achieving a larger absolute peak depolarization, as opposed to stimulation in the inward direction (Rall, 1964). This effect is maximized when the output sites are not intermingled with inputs within the same compartment (Fig. 5D, E, I). If they were intermingled, the voltage drive of inputs close to the release sites dominates, thereby masking any slow accumulation of depolarization from more distal synapses. Thus, the separation of inputs and outputs is a global dendritic strategy used to compute motion direction (Fig. 1A).

The second feature, the “end effect”, is the property of the closed end of the dendritic compartment that essentially reflects current flow in the outward direction and leads to less voltage attenuation in the direction of the distal compartment. This is in contrast to locations near branch points or the soma, which act as current sinks. The end effect is critical for ensuring that large segments of dendrite containing release sites are subjected to a similar depolarization, despite the increased distance from the last activated input, which in turn leads to a large region of the dendrite exhibiting DS (Fig. 5). This could also be a mechanism for synchronizing release from varicosities at different distances from the end of the dendrite.

In this study, we created a simulation based on passive membrane properties to examine the role of the excitatory input distribution. The principle prediction is that direction selectivity of distal dendritic voltage is enhanced if inputs are segregated away from release sites (Fig. 5). We confirmed this enhancement by monitoring calcium responses to motion stimuli as a proxy for voltage integration at release sites (Fig. 6). However, it is difficult to test empirically whether the alternative case, the regular distribution of inputs located all along the dendrite, produces weaker DS at release sites. Therefore it remains to be shown directly that exclusion of synaptic inputs near release sites is necessary, as our simulations suggest, to produce DS at most of the release sites.

It is likely that non-linearities also contribute to DS. SACs express the voltage-gated potassium channel Kv3.1, which is localized to proximal dendrites and which probably enhances the electrical isolation of dendrites pointing in different directions (Ozaita et al., 2004). SACs also exhibit TTX-insensitive voltage-gated sodium channel conductances (Oesch and Taylor, 2010), which might amplify the direction selective voltage observed in our model (Fig. 5). Voltage-gated Ca^{2+} channels could also amplify direction selective voltage—both P/Q and N-type channels are expressed in SACs (Lee et al., 2010; Xu et al., 2003) and adding voltage-gated Ca^{2+} channels to the varicosities in our model resulted in a significant amplification of DS in SAC varicosities (data not shown). Our evidence of the presence of nonlinearities is that we observe an outward preference of the somatic voltage in response to moving square stimuli, while a purely passive model would predict a small inward direction preference for voltage recorded at the soma (Fig. S5; Euler et al., 2002; Gavrikov et al., 2003, 2006; Hausselt et al., 2007; Oesch and Taylor, 2010; Ozaita et al., 2004). Directly measuring voltage in SAC dendrites would provide a basis for determining the contribution of each non-linearity to the amplification of passive DS. Finally, the cooperative binding of neurotransmitter release sensors (e.g. Kochubey et al., 2009) will likely contribute to amplification of DS release of GABA onto DSGCs.

A unifying model of SAC DS

So far, three models of how DS arises in SAC dendrites have been proposed. First, the space-time wiring model by Kim et al. (2014) proposes that bipolar cells with phasic vs. sustained release kinetics synapsing onto different regions of the dendrite produce a delay-line computation of DS. As shown in Figure S1, our voltage clamp recordings do not show detectable differences in bipolar cell release kinetics at different sites along the dendrite. However, the ideal experiment to test this model would be to record from bipolar cell-SAC pairs to test directly for differences in release kinetics.

Second, the lateral inhibition model postulates that DS in SACs arises due to lateral inhibition from other SACs. SACs release GABA onto one another (Kostadinov and Sanes, 2015; Lee and Zhou, 2006; Zheng et al., 2004) and a previous study demonstrated that the DS of Ca^{2+} responses in proximal varicosities requires surround stimulation in rabbit SACs (Lee and Zhou, 2006). This inhibition mechanism relies on the ability of GABA receptor activation to shunt excitation when inhibition arrives first (Münch and Werblin, 2006). However, other studies in rabbit retina have found that blocking GABA receptors did not affect direction selective responses in one example of dendritic Ca^{2+} imaging (Euler et al., 2002) or in direction selective responses as measured by voltage clamp recordings at the soma (Hausselt et al., 2007; Oesch and Taylor, 2010).

We found that lateral inhibition enhanced, but was not required for, DS in distal varicosities (Fig. 7). First, stimulating out to 100% of the dendritic tree, which maximally stimulates antiparallel presynaptic SAC processes, led to a larger DS than stimulation to 75% of the dendritic tree. Second, blockade of $GABA_A$ signaling reduced DS in distal varicosities, primarily by increasing the dendritic response to inward motion. It is important to note that a bath application of gabazine not only affects SAC-SAC interactions, but will also affect wide-field amacrine cell inputs to SACs (Hoggarth et al., 2015) as well as the amount of

glutamate released from bipolar cells, due to a relief of synaptic inhibition (Pei et al., 2015). However, GABA release from wide-field amacrine cells should not be DS, and the distribution of bipolar cell inputs on SACs allows them to maintain DS despite potential increases in glutamate release.

Our data are more in favor of a third model in which DS arises through a dendrite-intrinsic mechanism. In this model, the excitatory input distribution and passive cable properties described here contribute to the direction selectivity of dendritic voltage, and hence synaptic output. In addition, the differential distribution of inputs and outputs contributes to a circuit-based mechanism of DS in which lateral inhibition from neighboring SACs enhances DS. Overall, our findings suggest a model where the dendrite-intrinsic direction preference is enhanced by lateral inhibition from other SACs, a circuit-level interaction that itself requires the presence of the dendrite-intrinsic mechanism, leading to robust DS in SAC processes (Fig. S7).

Experimental Procedures

Details may be found in the **Extended Experimental Procedures**.

Visual stimulation and calcium imaging

To record from On-layer SACs, we used retinas from two mouse lines that express fluorescent proteins in SACs: *mGluR2-GFP* mice and *ChAT-Cre/nGFP* mice. For some experiments, wild-type (C57BL/6J; Jackson Labs) mice were used. Whole cell recordings were performed in Ames media using a cesium internal for voltage clamp and a potassium internal for Ca^{2+} imaging. Cells were targeted using IR illumination and 2-photon microscopy (Wei et al., 2010). 2-photon imaging used a custom-built microscope tuned to 810 nm (for Alexa-594 dye imaging) or 930 nm (for GFP and OGB-1 imaging). Visual stimuli were generated using a computer running either a monochromatic organic light-emitting display or a DMD projector with an LED light source. Stimuli were presented in pseudorandom order. Light intensity of visual stimuli ranged from 1.9–2.9 × 10^5 R*/rod/s.

Glutamate Uncaging

Retinas were prepared as described for visual stimulation (above) with the exception that dissections of wild-type mice were done in ambient light and tissue was stored in oxygenated ACSF. Voltage clamp recordings used either a cesium or potassium-based internal. Dendritic arbors were imaged using a custom 2-photon microscope tuned to 810 nm. The caged compound 4-methoxy-7-nitroindolinyl-caged L-glutamate (MNI-glutamate, Tocris Bioscience) was bath applied at a concentration of 2 mM (in ACSF) and glutamate was uncaged using a 405 nm laser with power = 2.55 mW.

PSD95 Labeling and Imaging

Retinas from mice of postnatal day 22 were labeled via biolistic transfection with PSD95-YFP and tdTomato using a cytomegalovirus (CMV) promoter driving expression of tandem dimer Tomato (tdTomato) or postsynaptic density protein 95 fused to yellow fluorescent protein (PSD95YFP) (Morgan and Kerschensteiner, 2012) using a Helios Gene Gun (Bio-

Rad) and then incubated for 24 hr. Afterwards, retinas were fixed in 4% paraformaldehyde in mACSF, rinsed in PBS, and flat mounted in Vectashield (Vector Laboratories) for confocal imaging on an Olympus FV-1000 laser scanning confocal microscope. SAC dendrites were skeletonized using Imaris (Bitplane). Potential PSD95YFP puncta were identified using custom MATLAB scripts previously described (Morgan et al., 2008). The log ratio of YFP to tdTomato fluorescence was calculated within each punctum (Torborg and Feller, 2004), (see Fig. S4 for details).

Simulation of SAC

Passive cable simulations of EPSC propagation or EPSP integration within an idealized SAC model were performed using Neuron v7.3 (Carnevale and Hines, 2006).

Data Analysis

Data analysis was performed in IgorPro (WaveMetrics) running Neuromatic functions, ImageJ, FIJI, Imaris, and MATLAB. The direction selectivity index is as follows (with direction of visual stimulation relative to SAC soma indicated by the subscript):

$$\frac{\frac{\Delta F}{F_{\text{out}}} - \frac{\Delta F}{F_{\text{in}}}}{\frac{\Delta F}{F_{\text{out}}} + \frac{\Delta F}{F_{\text{in}}}}$$

Supplementary Material

Refer to Web version on PubMed Central for supplementary material.

Acknowledgments

We are grateful to Kevin Briggman for providing previously published SBEM data, members of the Feller lab and DiGregorio lab for discussion and technical support, Rachel Wong for helpful comments on the manuscript and Melissa Panlasigui for microscopy support. ALV and RDM were supported by NSF Grant No. DGE 1106400 and ALV received support from NIH F31 NS089197-01. MBF, RDM, and ALV were supported by NIH ROI1EY019498, RO1EY013528 and P30EY003176. AB was supported by NIH EY10699. ALV, ATVM and DD were supported by the French National Agency for Research (ANR-2010-BLANC-1411, ANR-13-SAMA-0006-05, ANR-13-BSV4-0016) and the Fondation de Recherche Medicale (Team grant). ATVM and MBF were also supported by the Ecole des Neurosciences de Paris, and ATVM was also supported by a EMBO Long-Term Fellowship 1582–2011, a Roux-Howard-Cantarini post-doctoral fellowship and a Marie Curie Individual Fellowship 301362 within the 7th European Community Framework Program (FP7-PEOPLE-2011-IEF). CFG was supported by P30EY003176. This work received support from the France-Berkeley Fund.

References

Abrahamsson T, Cathala L, Matsui K, Shigemoto R, Digregorio DA. Thin dendrites of cerebellar interneurons confer sublinear synaptic integration and a gradient of short-term plasticity. Neuron. 2012; 73:1159–1172. [PubMed: 22445343]

Amthor FR, Keyser KT, Dmitrieva NA. Effects of the destruction of starburst-cholinergic amacrine cells by the toxin AF64A on rabbit retinal directional selectivity. Vis. Neurosci. 2002; 19:495–509. [PubMed: 12511082]

Beier KT, Borghuis BG, El-Danaf RN, Huberman a. D, Demb JB, Cepko CL. Transsynaptic Tracing with Vesicular Stomatitis Virus Reveals Novel Retinal Circuitry. J. Neurosci. 2013; 33:35–51. [PubMed: 23283320]

Berntson A, Taylor WR. Response characteristics and receptive field widths of on-bipolar cells in the mouse retina. J. Physiol. 2000; 524:879–889. [PubMed: 10790165]

Briggman KL, Helmstaedter M, Denk W. Wiring specificity in the direction-selectivity circuit of the retina. Nature. 2011; 471:183–188. [PubMed: 21390125]

Carnevale, NT.; Hines, ML. The NEURON book. Cambridge, UK: Cambridge University Press; 2006.

Chen M, Lee S, Park SJH, Looger LL, Zhou ZJ. Receptive field properties of bipolar cell axon terminals in the direction-selective sublaminas of the mouse retina. J. Neurophysiol. 2014

DiGregorio DA, Rothman JS, Nielsen TA, Silver RA. Desensitization properties of AMPA receptors at the cerebellar mossy fiber granule cell synapse. J. Neurosci. 2007; 27:8344–8357. [PubMed: 17670981]

Euler T, Detwiler PB, Denk W. Directionally selective calcium signals in dendrites of starburst amacrine cells. Nature. 2002; 418:845–852. [PubMed: 12192402]

Famiglietti EV. Synaptic organization of starburst amacrine cells in rabbit retina: analysis of serial thin sections by electron microscopy and graphic reconstruction. J. Comp. Neurol. 1991; 309:40–70. [PubMed: 1894768]

Fried SI, Münch Ta, Werblin FS. Mechanisms and circuitry underlying directional selectivity in the retina. Nature. 2002; 420:411–414. [PubMed: 12459782]

Fried SI, Münch Ta, Werblin FS. Directional selectivity is formed at multiple levels by laterally offset inhibition in the rabbit retina. Neuron. 2005; 46:117–127. [PubMed: 15820698]

Gavrikov KE, Dmitriev AV, Keyser KT, Mangel SC. Cation-chloride cotransporters mediate neural computation in the retina. Proc. Natl. Acad. Sci. U. S. A. 2003; 100:16047–16052. [PubMed: 14665697]

Gavrikov KE, Nilson JE, Dmitriev AV, Zucker CL, Mangel SC. Dendritic compartmentalization of chloride cotransporters underlies directional responses of starburst amacrine cells in retina. Proc. Natl. Acad. Sci. U. S. A. 2006; 103:18793–18798. [PubMed: 17124178]

Hausselt SE, Euler T, Detwiler PB, Denk W. A dendrite-autonomous mechanism for direction selectivity in retinal starburst amacrine cells. PLoS Biol. 2007; 5:e185. [PubMed: 17622194]

Hoggarth A, McLaughlin AJ, Ronellenfitch K, Trenholm S, Vasandani R, Sethuramanujam S, Schwab D, Briggman KL, Awatramani GB. Specific Wiring of Distinct Amacrine Cells in the Directionally Selective Retinal Circuit Permits Independent Coding of Direction and Size. Neuron. 2015; 86:276–291. [PubMed: 25801705]

Kim JS, Greene MJ, Zlateski A, Lee K, Richardson M, Turaga SC, Purcaro M, Balkam M, Robinson A, Behabadi BF, et al. Space-time wiring specificity supports direction selectivity in the retina. Nature. 2014; 509:331–336. [PubMed: 24805243]

Kochubey O, Han Y, Schneggenburger R. Developmental regulation of the intracellular Ca2+ sensitivity of vesicle fusion and Ca2+-secretion coupling at the rat calyx of Held. J. Physiol. 2009; 587:3009–3023. [PubMed: 19403608]

Koizumi A, Jakobs TC, Masland RH. Regular mosaic of synaptic contacts among three retinal neurons. J. Comp. Neurol. 2011; 519:341–357. [PubMed: 21165978]

Kostadinov D, Sanes JR. Protocadherin-dependent dendritic self-avoidance regulates neural connectivity and circuit function. Elife. 2015; 4:1–23.

Lee S, Zhou ZJ. The synaptic mechanism of direction selectivity in distal processes of starburst amacrine cells. Neuron. 2006; 51:787–799. [PubMed: 16982423]

Lee S, Kim K, Zhou ZJ. Role of ACh-GABA cotransmission in detecting image motion and motion direction. Neuron. 2010; 68:1159–1172. [PubMed: 21172616]

Morgan JL, Kerschensteiner D. Coating gold particles with DNA (biolistics). Cold Spring Harb. Protoc. 2012; 2012:114–117. [PubMed: 22194253]

Morgan JL, Schubert T, Wong ROL. Developmental patterning of glutamatergic synapses onto retinal ganglion cells. Neural Dev. 2008; 3:8. [PubMed: 18366789]

Morrie RD, Feller MB. An Asymmetric Increase in Inhibitory Synapse Number Underlies the Development of a Direction Selective Circuit in the Retina. J. Neurosci. 2015; 35:9281–9286. [PubMed: 26109653]

Münch, Ta; Werblin, FS. Symmetric interactions within a homogeneous starburst cell network can lead to robust asymmetries in dendrites of starburst amacrine cells. J. Neurophysiol. 2006; 96:471–477. [PubMed: 16598066]

Oesch NW, Taylor WR. Tetrodotoxin-resistant sodium channels contribute to directional responses in starburst amacrine cells. PLoS One. 2010; 5:e12447. [PubMed: 20805982]

Ozaita A, Petit-Jacques J, Völgyi B, Ho CS, Joho RH, Bloomfield Sa, Rudy B. A unique role for Kv3 voltage-gated potassium channels in starburst amacrine cell signaling in mouse retina. J. Neurosci. 2004; 24:7335–7343. [PubMed: 15317859]

Park SJH, Kim I-J, Looger LL, Demb JB, Borghuis BG. Excitatory synaptic inputs to mouse on-off direction-selective retinal ganglion cells lack direction tuning. J. Neurosci. 2014; 34:3976–3981. [PubMed: 24623775]

Pei Z, Chen Q, Koren D, Giammarinaro B, Acaron Ledesma H, Wei W. Conditional Knock-Out of Vesicular GABA Transporter Gene from Starburst Amacrine Cells Reveals the Contributions of Multiple Synaptic Mechanisms Underlying Direction Selectivity in the Retina. J. Neurosci. 2015; 35:13219–13232. [PubMed: 26400950]

Rall W. Theoretical significance of dendritic trees for neuronal input-output relations. Neural Theory Model. 1964:73–97.

Rall W. Distinguishing theoretical synaptic potentials computed for different soma-dendritic distributions of synaptic input. J. Neurophysiol. 1967; 30:1138–1168. [PubMed: 6055351]

Taylor WR, Smith RG. The role of starburst amacrine cells in visual signal processing. Vis. Neurosci. 2012; 29:73–81. [PubMed: 22310373]

Torborg CL, Feller MB. Unbiased analysis of bulk axonal segregation patterns. J. Neurosci. Methods. 2004; 135:17–26. [PubMed: 15020085]

Tukker JJ, Taylor WR, Smith RG. Direction selectivity in a model of the starburst amacrine cell. Vis. Neurosci. 2004; 21:611–625. [PubMed: 15579224]

Vaney DI, Sivyer B, Taylor WR. Direction selectivity in the retina: symmetry and asymmetry in structure and function. Nat. Rev. Neurosci. 2012; 13:194–208. [PubMed: 22314444]

Vlasits AL, Bos R, Morrie RD, Fortuny C, Flannery JG, Feller MB, Rivlin-Etzion M. Visual Stimulation Switches the Polarity of Excitatory Input to Starburst Amacrine Cells. Neuron. 2014; 83:1172–1184. [PubMed: 25155960]

Wei W, Elstrott J, Feller MB. Two-photon targeted recording of GFP-expressing neurons for light responses and live-cell imaging in the mouse retina. Nat. Protoc. 2010; 5:1347–1352. [PubMed: 20595962]

Wei W, Hamby AM, Zhou K, Feller MB. Development of asymmetric inhibition underlying direction selectivity in the retina. Nature. 2011; 469:402–406. [PubMed: 21131947]

Xu H, Zhao J, Yang X. Cholinergic and dopaminergic amacrine cells differentially express calcium channel subunits in the rat retina. Neuroscience. 2003; 118:763–768. [PubMed: 12710983]

Yonehara K, Balint K, Noda M, Nagel G, Bamberg E, Roska B. Spatially asymmetric reorganization of inhibition establishes a motion-sensitive circuit. Nature. 2011; 469:407–410. [PubMed: 21170022]

Yonehara K, Farrow K, Ghanem A, Hillier D, Balint K, Teixeira M, Jüttner J, Noda M, Neve RL, Conzelmann K-K, et al. The First Stage of Cardinal Direction Selectivity Is Localized to the Dendrites of Retinal Ganglion Cells. Neuron. 2013; 79:1–8. [PubMed: 23849191]

Yoshida K, Watanabe D, Ishikane H, Tachibana M, Pastan I, Nakanishi S. A key role of starburst amacrine cells in originating retinal directional selectivity and optokinetic eye movement. Neuron. 2001; 30:771–780. [PubMed: 11430810]

Zheng J, Lee S, Zhou Z. A Developmental Switch in the Excitability and Function of the Starburst Network in the Mammalian Retina. Neuron. 2004; 44:851–864. [PubMed: 15572115]

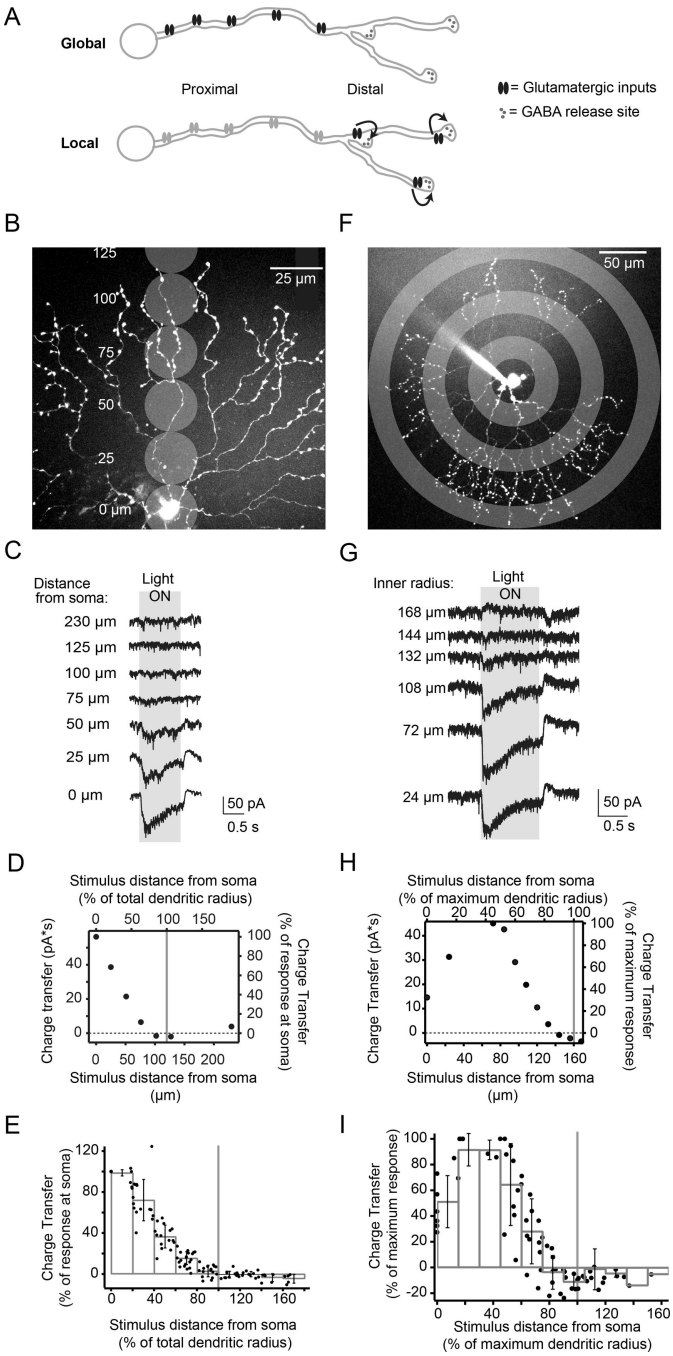

Figure 1. Starburst amacrine cell excitatory receptive field is smaller than dendritic field

A) Schematic of two distributions of glutamatergic inputs (ovals) and GABAergic release sites (outputs, small circles) on a SAC dendrite. The skewed distribution (top) produces a global computation where all inputs contribute, while the regular distribution produces primarily local computations, with receptors near outputs having a dominant effect on neurotransmitter release (arrows).

B) Schematic showing locations of visual stimulation spots overlaid on a 2-photon fluorescence image of a SAC (z-projection). Distances are relative to the soma.

C) Light-evoked current responses for illumination locations shown in **B** (holding potential = −72 mV). Grey box indicates the timing of the stimulus onset and offset. Traces are averages of 4 sweeps.

D) Excitatory charge transfer as a function of distance from experiment in **C**. Right and top axes are normalized to the maximum charge transfer and maximum dendritic radius, respectively. Grey vertical line: the radius of the dendritic tree.

E) Normalized excitatory charge transfer following visual stimulation as a function of distance from the soma (15 cells). Black dots: individual cells; grey bars: binned averages. Grey vertical line: 100% of the radius of the dendritic tree. Error bars = S.D.

F) Schematic showing anatomical location of visual stimulation rings overlaid with 2-photon fluorescence projection of a SAC at low magnification. Rings shown have an inner radius of 24, 72, and 132 μm. The thickness of the rings was 24 μm.

G) Voltage clamp recordings (holding potential = −72 mV) from the SAC in **F** during stimulation with stationary rings (width = 24 μm) with different inner radii. Averages of 4 sweeps. Grey box: the timing of the stimulus onset and offset.

H) Excitatory charge transfer calculated from the recordings in **G** plotted as a function of the inner radius from the soma. Right and top axes are normalized to the maximum charge transfer and maximum dendritic radius, respectively. For this cell, the maximum dendritic radius was 160 μm.

I) Excitatory charge transfer calculated for 6 cells plotted as a function of the length of the inner radius from the soma. Axes are normalized to the maximum charge transfer response and maximum dendritic radius, respectively. Black dots: measurements from each cell; grey bars: binned averages of these measurements; error bars: S.D.

See also Figure S1.

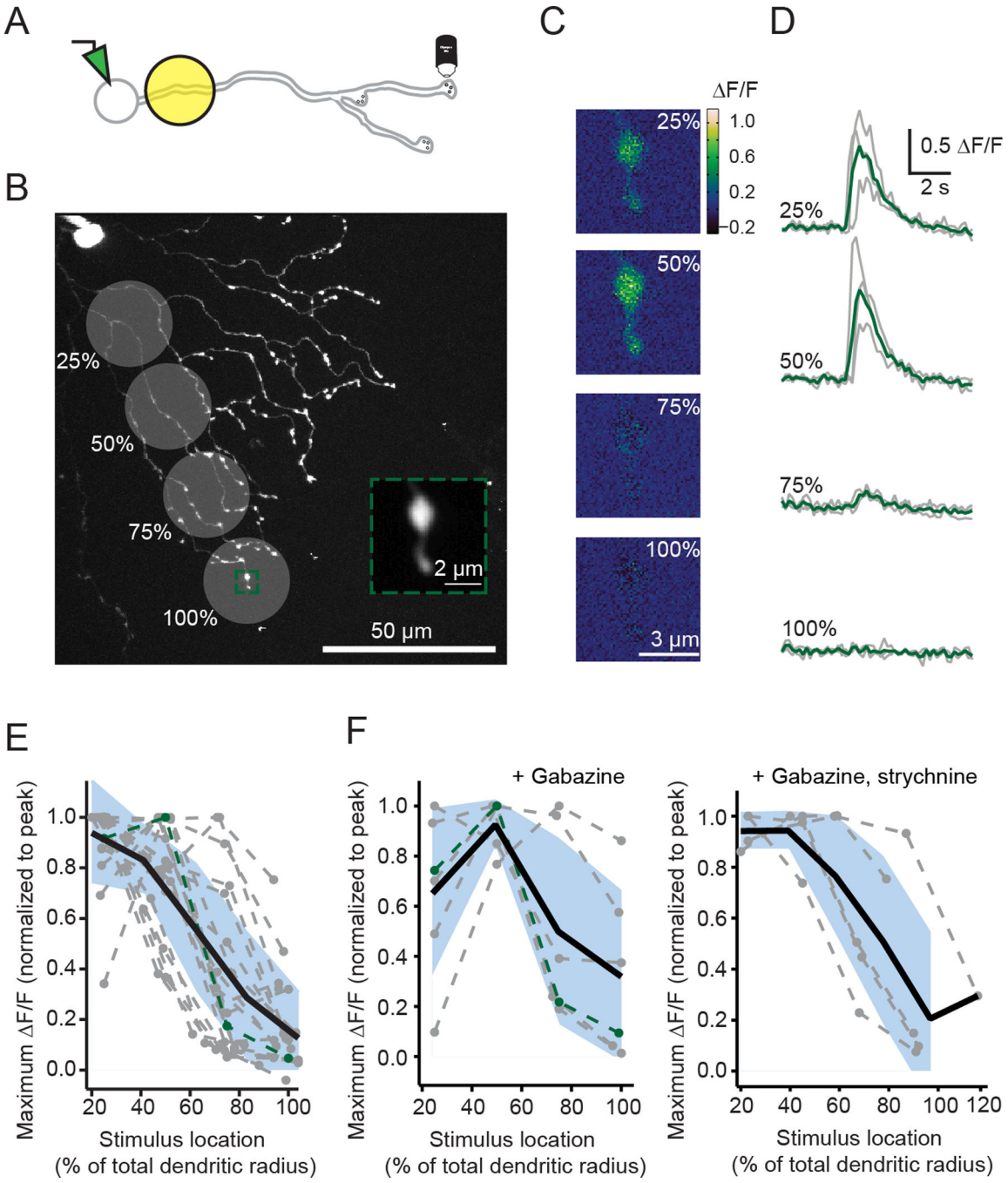

Figure 2. Ca^{2+} transients in varicosities are largest during proximal visual stimulation

A) Schematic displaying experiment to image a distal varicosity from a SAC filled with 150 µM OGB-1 during visual stimulation with 25 µm diameter spots.

B) Location of visual stimulation spots overlaid with a 2-photon fluorescence image of a SAC filled with OGB-1 (z-projection). Visual stimuli were centered at indicated positions (25, 50, 75, 100%) after measuring the SAC dendritic radius along the axis of the varicosity being imaged. Green box: ROI used to image a distal varicosity. The soma and patch

electrode are visible in the top left corner. Inset: average intensity projection of the fluorescent images acquired during visual stimulation.

C) Maximal change in fluorescence (ΔF/F) responses of the ROI shown in **B** to one presentation of each spot located at the indicated % of the total dendritic radius along the axis of the varicosity being imaged.

D) ΔF/F (grey lines) following visual stimulation centered at the % of the total dendritic radius for the varicosity in **B**. Green traces: the mean of three trials.

E) Maximum ΔF/F normalized to the peak response for 15 varicosities measured from 15 cells in response to stimuli at four locations along their dendrites (grey dotted lines; green line = the cell in **B–D**). Black line: the average response of linear interpolations of each receptive field. Blue shading = S.D.

F) Same as **E** but for varicosities in the presence of 5 μM gabazine (left; 5 cells) or 5 μM gabazine + 1 μM strychnine (right; 5 cells) to isolate the excitatory inputs.

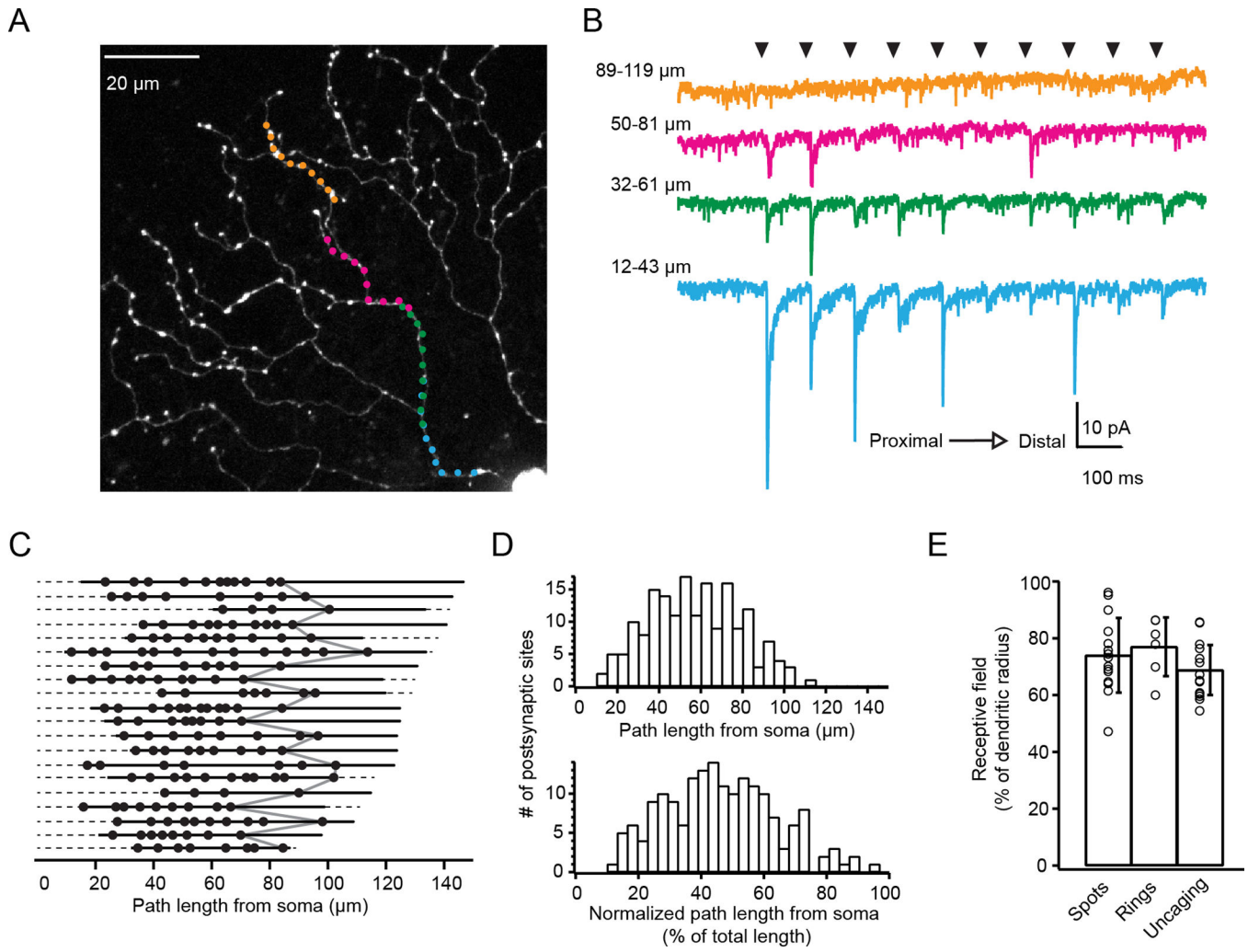

Figure 3. Glutamate receptors are absent from distal dendrites

A) 2-photon fluorescence image of a SAC (z-projection) with targeted locations of glutamate uncaging sites along one dendritic path. Colors correspond to current responses in **B**.

B) Voltage clamp recordings (holding potential = −72 mV) from the cell in **A** in response to glutamate uncaging at 40 dendritic sites. Black arrowheads indicate the timing of the 100 µs laser uncaging pulses at different dendritic sites (moving outward from the soma to the distal dendrites from left to right and bottom to top). Traces are averages of 10 sweeps.

C) Locations where uncaging-evoked EPSCs indicated the presence of putative postsynaptic sites (black dots). Each row represents a different dendrite (n = 20 dendrites from 15 cells). Dashed lines: the entire path lengths from the soma to the end of the dendrite; solid lines: the path lengths sampled by uncaging. Locations of the last synapses in each dendrite are connected by the grey line.

D) Histograms of the putative postsynaptic sites as a function of path length (top) or path length normalized to the dendritic length of each dendrite.

E) Starburst amacrine cell excitatory receptive field size determined using spot stimulation (‘Spots’), ring stimulation (‘Rings’), or glutamate uncaging (‘Uncaging’). Error bars are S.D.

See also Figures S2–3.

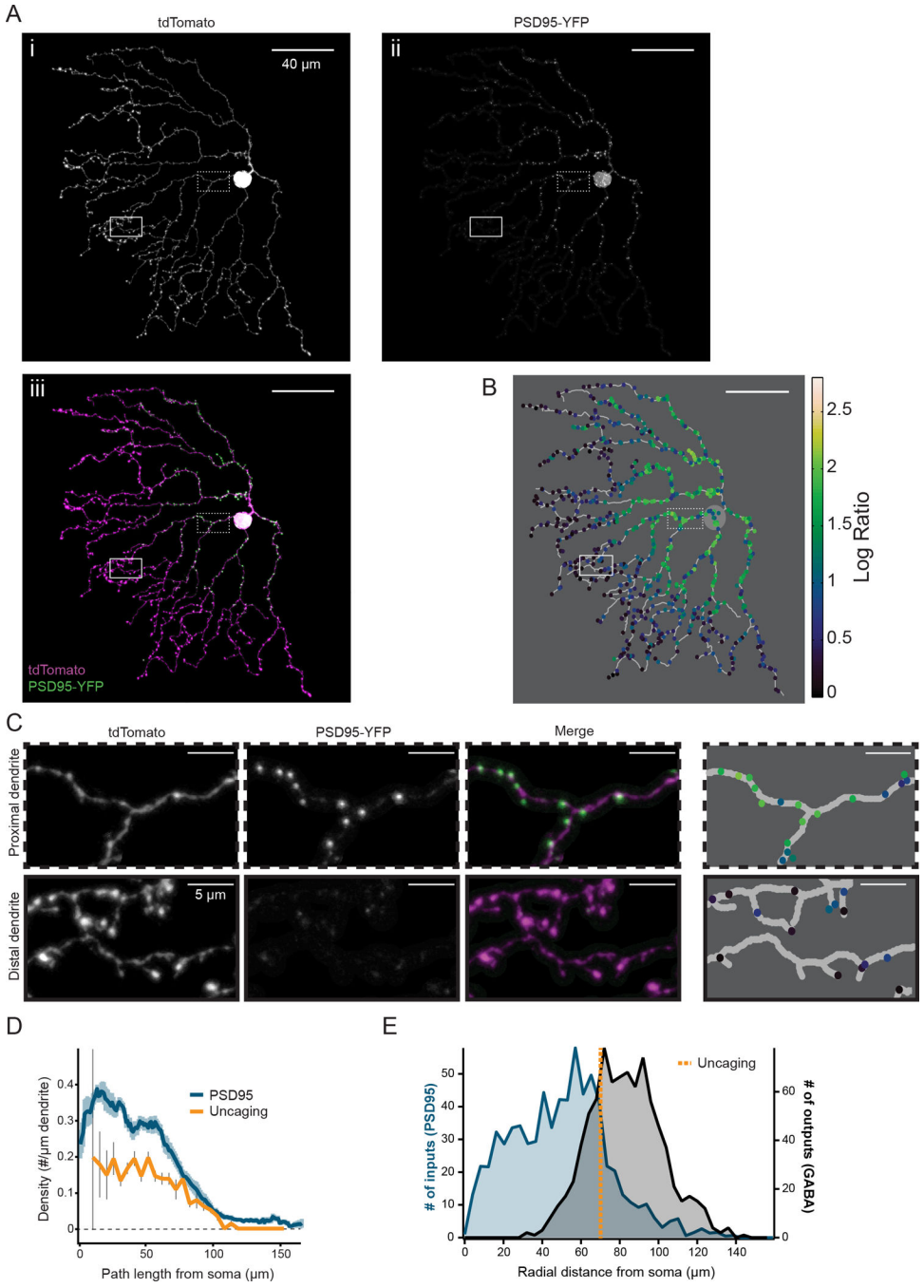

Figure 4. Distribution of putative postsynaptic sites is skewed away from output sites

A) Projection image of the analyzed dendritic processes of a SAC expressing tdTomato (**i**) and PSD95-YFP (**ii**). **iii** is a merged image showing tdTomato in magenta and PSD95-YFP in green; in this image, contrast was adjusted to improve visibility for display. The image was masked to exclude dendritic branches that overlapped with other labeled cells to ensure that only PSD95 puncta from SACs were included in analysis. Magnified regions (dotted and solid boxes) correspond to example proximal and distal regions in **C**.

B) Skeleton of cell from **A** with identified PSD95 puncta (colored dots). Colors represent the log ratio of the PSD95 to tdTomato fluorescence intensity within each puncta, which was used for thresholding puncta to include in subsequent analysis (see Methods).
C) Examples of proximal (top) and distal (bottom) regions indicated by the dotted and solid boxes in **A**. Colors of identified puncta in the 4th column correspond to the heat map in **B**.
D) Density of PSD95-YFP puncta or putative postsynaptic sites determined by uncaging (see Fig. 3E) as a function of dendritic path length from the soma. For PSD95, the average linear density of PSD95 puncta using a 10 μm sliding window is plotted using a threshold log ratio of 1.0 to select puncta to include (blue line; light blue shading = S.E.M, 8 cells). For uncaging, histogram of the average density of putative postsynaptic sites in 5 μm bins is plotted (orange line; grey bars = S.E.M, 23 dendrites).
E) Histogram of PSD95 puncta from 8 SACs using a threshold log ratio of 1.0 (left axis, blue) as well as the synaptic contacts with DSGCs (outputs, right axis, black) as a function of radial distance from the soma. Orange dotted line: the mean radial distance of the last putative postsynaptic sites detected with uncaging (see Fig. 3E). Outputs were determined from electron microscopy reconstructions of 24 SACs (Briggman et al., 2011) and analyzed as a function of radial distance to compare with PSD95 locations.
See also Figure S4.

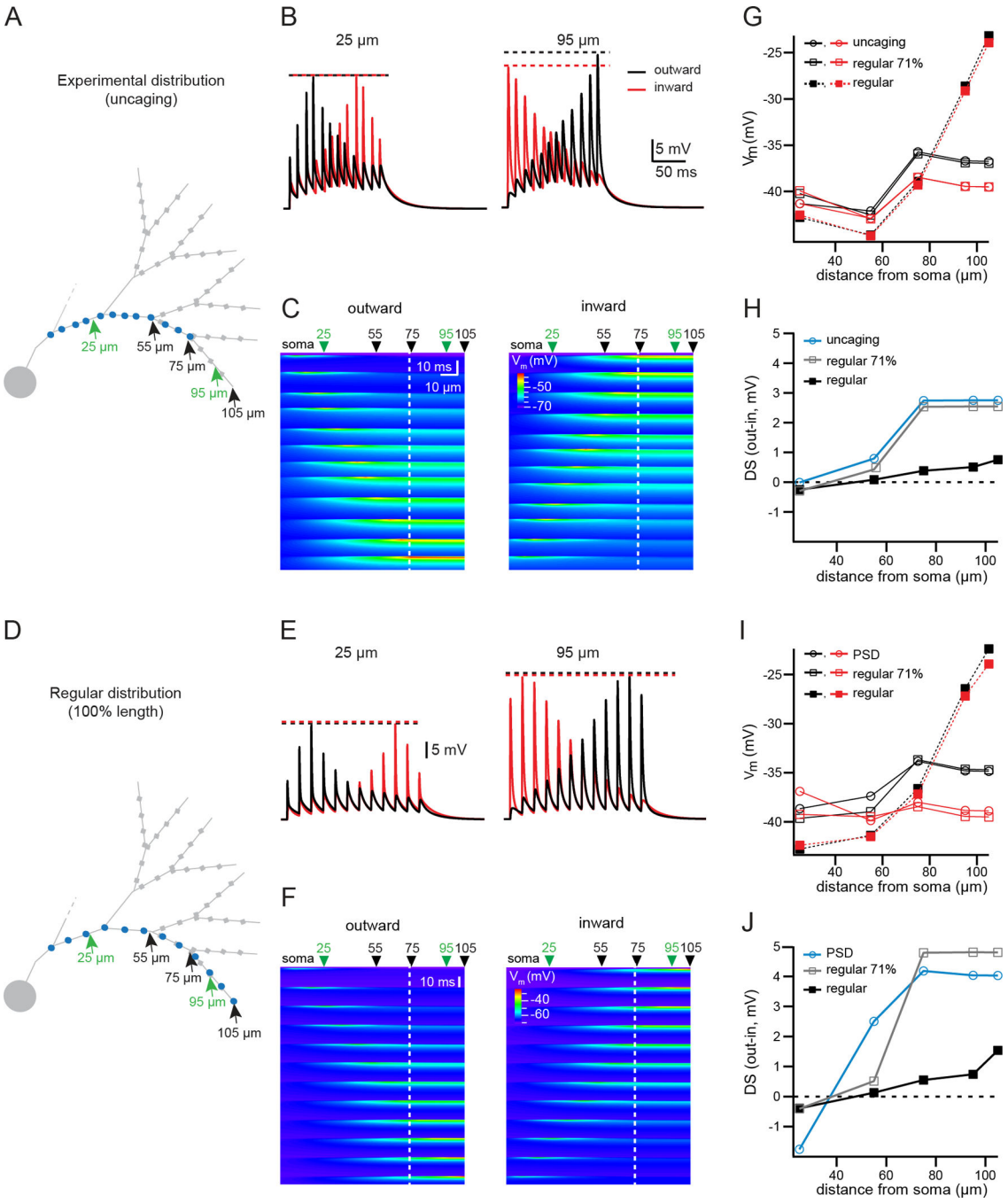

Figure 5. Synaptic input distribution supports DS of simulated dendritic voltage

A) Ball-and-stick representation of a partial SAC dendritic tree, used for simulations of dendritic integration in a passive model. Blue circles: the location of synapses used in simulations, corresponding to the average location of putative synapses determined from uncaging. Green arrows: locations where the dendritic voltage is plotted in **B**; black arrows: locations where the peak of the dendritic voltage is plotted in the summary in **G–H**. Grey squares: wider compartments of the distal dendrite representing varicosities.

B) Simulated dendritic voltage at two locations (indicated by green arrows in **A**), in response to the outward (black traces) or inward (red traces) activation of the synapses displayed in **A** at a speed of 500 μm/s. Dotted lines: amplitude of the peak of the synaptic response in each condition.

C) Heat map of simulated dendritic voltage measured along the entire dendritic branch containing the activated synapses (x-axis) for the duration of the stimulus (y-axis). The color scale depicts the peak amplitude of the depolarization. *Left plot*: response to outward stimulation. *Right plot*: response to inward stimulation. At the peak of the activation of each synapse, the local voltage propagates with little electrotonic attenuation to the dendritic tip due to the end effect of the electrical cable. Green arrows: the two positions along the dendrite corresponding to the traces in **B** (25 and 95 μm from the soma); black arrows: locations where the peak of the dendritic voltage is plotted in the summary in **G–H**. The white dotted line indicates the location of the most distal synapse.

D) Same as **A**, but blue circles indicate the location of regularly distributed synapses, the most distal synapse being located at the tip of the dendrite. For the regular distributions, the average density is the same as the experimental distribution determined with uncaging (0.09/μm).

E) Same as **B**, for the gradient of regular synapses stopping at 100% of the dendritic length (displayed in **D**).

F) Same as **C**, for the gradient of regular synapses stopping at 100% of the dendritic length (displayed in **D**).

G) Plot of the maximum simulated dendritic voltage during inward (red) or outward (black) activation of synapses, measured at several dendritic locations, for the experimental distribution of synapses (circles, solid lines), a distribution of regularly spaced synapses with the most distal synapse located at 71% of the length of the dendrite as in the experimental distribution (open squares, solid lines), and the regular distribution stopping at the tip of the dendrite (closed squares, dotted lines).

H) Summary plot showing the DS (defined as the difference of the peak dendritic voltage measured during outward and inward activation of inputs) at various dendritic locations for the different synaptic distributions (experimental distribution of synapses, circles, light blue; regularly spaced synapses with the most distal synapse located at 71% of the dendritic length, open squares, grey; regular distribution stopping at the tip of the dendrite, closed squared, black).

I) Same as **G**, using synapse gradients determined from the average locations of PSD95 labeling (see Fig. S5). The regular distributions in this plot have the same average synaptic density as the experimental distribution from PSD95 labeling (0.2/μm).

J) Same as **H**, using synapse gradients determined from the average locations of putative PSDs.

See also Figure S5.

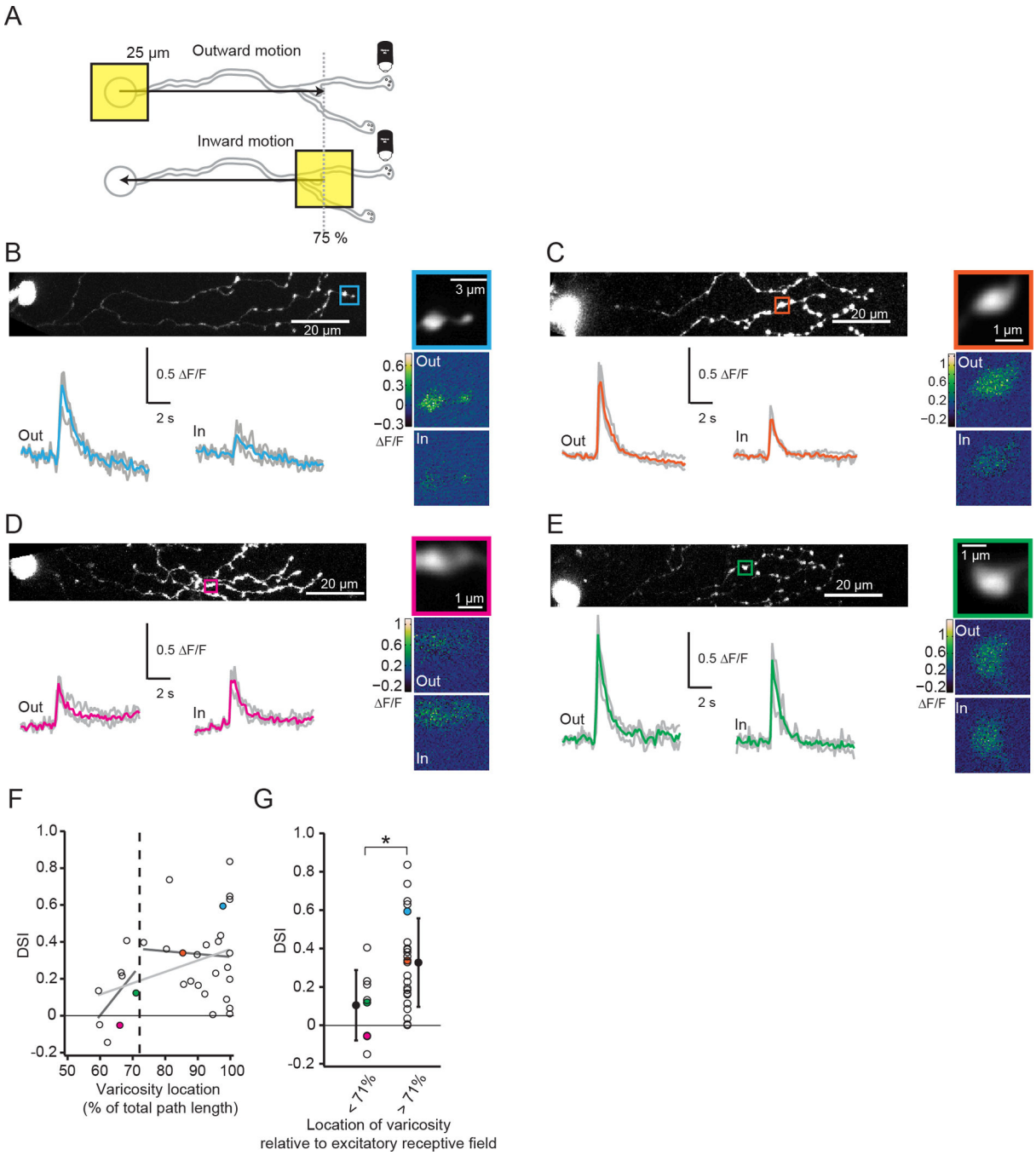

Figure 6. DS of varicosities depends on varicosity location

A) Schematic showing imaging of a distal varicosity from an OGB-1-filled SAC presented with a 25 µm square of light moving either outward from the soma toward the distal dendrites or inward from the distal dendrites toward the soma. The stimulus was restricted to 75% of the dendritic radius (grey dotted line).

B–E Four examples of Ca^{2+} responses to stimulation with moving squares. **B** is an example of an outward-preferring varicosity near the end of the dendrite. **C** is an example of a more

proximal varicosity that is strongly direction selective for outward motion. **D** is an example of a slightly inward-preferring varicosity. **E** is an example of an untuned varicosity.
Top left: 2-photon fluorescence image of SAC filled with OGB-1 (z-projection). The square indicates the imaged varicosity. The soma is on the left.
Top right: Average intensity projection of the imaged varicosity during the entire experiment.
Bottom left: ΔF/F (grey) following visual stimulation with a 25 μm moving square either outward from the soma toward the end of the dendrites ("out") or inward from the distal dendrites toward the soma ("in"). Colored traces: averages of the three trials.
Bottom right: Maximal ΔF/F responses of the imaged varicosities to a single presentation of the moving square moving outward ("out") or inward ("in") along the dendritic radius.
F) Direction selective index (DSI) for varicosities from 33 cells in response to inward vs. outward moving squares (black circles) as a function of the varicosity location normalized to the path length of the dendrite. A positive value for the DSI indicates a larger response for outward motion compared to inward motion. Colored dots are the DSIs for the example cells in **B–E**. Black dotted line: average length of the excitatory receptive field predicted from uncaging (see Fig. 3). Light grey line is a linear fit to the entire data set (slope = 0.006, r2 = 0.134) while dark grey lines are fits to the varicosities inside vs. outside of the receptive field detected from uncaging (inside: slope = 0.022, r2=0.248; outside: slope = −0.002, r2 = 0.002).
G) DSI for varicosities from 33 cells (black circles) sorted by whether they are within (< 71%; 8 cells) or outside (> 71%; 25 cells) of the mean excitatory receptive field predicted from uncaging (black dotted line in **F**). Colored dots are the DSIs for the example cells in **B–E**. Open circles = means ;error bars = S.D. * = $p < 0.05$, Student's t-test.
See also Figure S6.

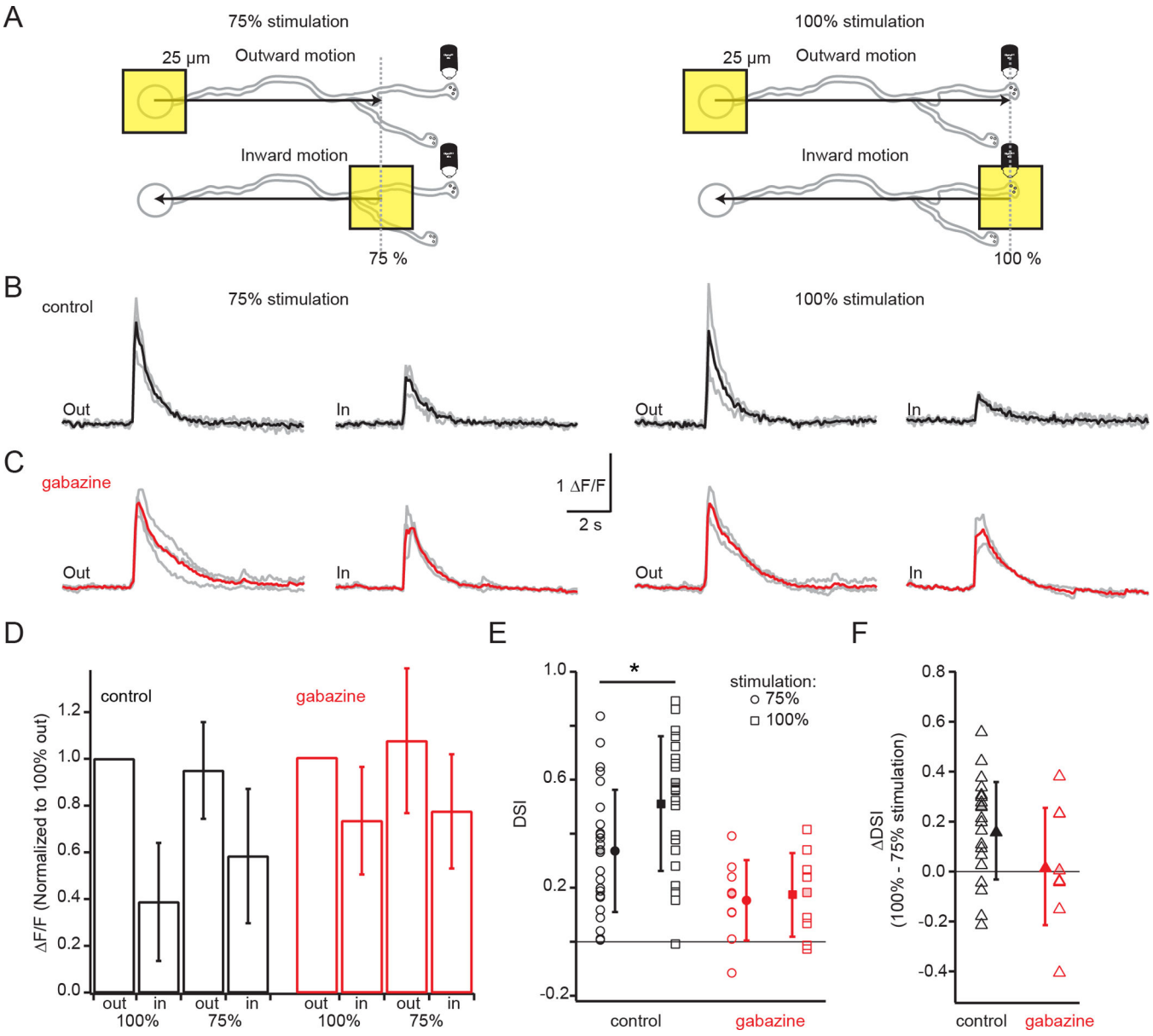

Figure 7. GABAergic lateral inhibition enhances DS

A) Schematic showing imaging of a distal varicosity from an OGB-1-filled SAC presented with a 25 µm square of light moving either outward from the soma toward the distal dendrites or inward from the distal dendrites toward the soma. *Left*: Visual stimulation restricted to 75% of the dendritic radius (grey dotted line), which activated less of the lateral inhibition from neighboring SACs. *Right*: Visual stimulation of 100% of the dendritic radius (grey dotted line), which activated more of the lateral inhibition.

B) Ca^{2+} responses (ΔF/F, grey) from a single varicosity following visual stimulation with a 25 µm moving square either outward from the soma toward the end of the dendrites ("out") or inward from the distal dendrites toward the soma ("in") in response to either the 75% stimulation (left traces) or the 100% stimulation (right traces) depicted in **A**. Black traces: averages of three trials.

C) Same as **B** but showing the responses of a different varicosity from a different cell in the presence of 5 μm gabazine to block $GABA_a$ receptors. Red traces: averages of the three trials.

D) The average maximum ΔF/F for varicosities in control conditions (black bars) in response to 100% (23 cells) or 75% (26 cells) outward and inward stimulation normalized to the response to 100% outward stimulation and in 5 μm gabazine (red, 9 cells for both 75% and 100% stimulation). The control and gabazine populations are separate. Error bars = S.D.

E) Direction selective index (DSI) for the varicosities in **D** in response to 75% stimulation (circles) or 100% stimulation (squares) in control conditions (black) or 5 μM gabazine (red). Solid symbols = mean; error bars = S.D. * = paired t-test: $p<0.05$, n=22 varicosities for which both 75% and 100% stimulation was measured. Shaded-in symbols: example cells in **B** and **C**.

F) The ΔDSI showing the difference between the DSI in response to 100% vs 75% stimulation in varicosities in control conditions (black triangles, 22 cells) and in 5 μm gabazine (red triangles, 9 cells). Solid triangles: means; error bars = S.D. Shaded-in symbols: example cells in **B** and **C**.

See also Figure S7.